Energy Storage Materials 52 (2022) 675–684

Contents lists available at ScienceDirect

Energy Storage Materials

journal homepage: www.elsevier.com/locate/ensm

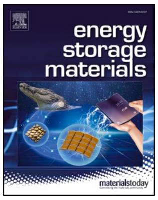

Inorganic manganese oxide/quinone coupling for high-capacity aqueous Zn-ion battery

Fei Ye [a], Qiang Liu [a], Chengjie Lu [a], Fanqi Meng [b], Ting Lin [b], Hongliang Dong [c], Lin Gu [b,*], Yuping Wu [d], Zilong Tang [e], Linfeng Hu [a,*]

[a] School of Materials Science and Engineering, Southeast University, No.2 Southeast University Road, Nanjing, Jiangsu 211189, China
[b] Beijing National Laboratory for Condensed Matter Physics, Institute of Physics, School of Physical Sciences, University of Chinese Academy of Sciences, Beijing, China
[c] Center for High Pressure Science and Technology Advanced Research, Shanghai 201203, China
[d] School of Energy and Environment, Southeast University, Nanjing 211189, China
[e] State Key Laboratory of New Ceramics and Fine Processing, School of Materials Science and Engineering, Tsinghua University, Beijing 100084, China

ARTICLE INFO

Keywords:
MnO_2@quinone
Inorganic/organic coupling
Specific capacity
Co-insertion mechanism
Dissolution/deposition mechanism

ABSTRACT

Rechargeable aqueous Zinc-ion batteries belong to a hot research topic on energy storage due to its high safety and low cost. However, its practical application is still remarkably limited by the fact that cathode capacity is much lower than that of zinc anode, leading to unsatisfactory energy density far away from the commercial standard. In this context, we have proposed an inorganic oxide/organic quinone coupling strategy to prepare MnO_2@PDAAQ composite cathode. Significantly enhanced performance superior to most of conventional cathode materials was identified in this MnO_2@PDAAQ with an impressive high capacity of 414 mAh g^{-1} and energy density of 537.9 Wh kg^{-1}. We clarified such a coupling from MnO_2 and quinone results in multiple energy storage mechanisms including Zn^{2+}/H^+ co-insertion in MnO_2 and two-electron dissolution/deposition mechanism of Mn^{4+}/Mn^{2+} redox reaction in this composite. The proposed inorganic oxide/organic quinone coupling strategy opens up a new route for the electrode design of high-performance aqueous batteries.

1. Introduction

Compared with the commercial lithium-ion batteries (LIBs), water-based rechargeable batteries have been emerged as very promising energy storage systems due to the high safety, low cost and much higher ionic conductivity (~ 1 S cm^{-1}) in aqueous electrolyte. Especially, aqueous Zn-ion batteries (ZIBs) has been considered as the most appealing alternative owing to its high volumetric capacity (5855 mAh cm^{-3} versus 2061 mAh cm^{-3} for Li), eco-friendliness and abundance of the zinc [1–4].

The main bottleneck of ZIBs development is on the lack of high-performance cathode materials. In general, the as-developed cathode materials can be classified as four types including Prussian blue analogues, V-based oxides, Mn-based oxides and organic compounds [5–11]. Among these materials, Prussian blue analogues and V-based oxides always deliver inferior specific capacity (< 60 mAh g^{-1}) and low voltage plateau (0.7 V vs. Zn/Zn^{2+}), respectively. Mn-based oxides deliver the best overall electrochemical performance on both capacity and working voltage [12,13]. Unfortunately, the capacity of Mn-based cathodes is still much lower than that of zinc anode, leading to the limited energy density of ZIBs that is still far away from the commercial standard. Therefore, enhancing the capacity of Mn-based cathode is the dominated route to break though the current bottleneck of aqueous ZIBs, and it is still highly challenging.

Most recently, many efforts have been reported in the field of coupling inorganic and organic materials to be applied as the cathode materials of AZIBs [7,14–16]. Generally, the selected organic species (mostly conducting polymers, e.g., PANI [7,14] and PEDOT [15]) can function as immobile pillars to enlarge the interlamellar spacing and enhance the electronic conductivity while they are polymerized in the interlayers. As the novel ZIBs cathode materials, organic quinone compounds (such as C4Q [17], PQ-Δ [18], PDBS [19] and TABQ [20]) with excellent structural diversity and potential resource sustainability has been paid more attention. The large intermolecular adjustable space and interaction forces (such as van der Waals forces, π-π forces, etc.) of quinone compounds provide an elastic substrate for reversible insertion/extraction of Zn^{2+} and promote the cationic diffusion process in electrolyte [21–24]. Motivation by these merits, we consider whether

---

* Corresponding authors.
E-mail addresses: l.gu@iphy.ac.cn (L. Gu), linfenghu@seu.edu.cn (L. Hu).

https://doi.org/10.1016/j.ensm.2022.08.040
Received 8 July 2022; Received in revised form 13 August 2022; Accepted 28 August 2022
Available online 29 August 2022

one can couple Mn-based oxides and organic quinone compounds together to produce novel inorganic oxide/organic composited cathode or not. However, such a consideration has never been reported up to date due to the lack of appropriate synthetic strategy.

Our previous work developed a series of manganese oxide nanodots as the promising prospective cathode candidates ZIBs [25]. Herein, we initially tried to realize the coupling inorganic MnO_2 and poly(1, 5-diaminoanthraquinone) (denoted as MnO_2@PDAAQ) through an interfacial polymerization method as cathode material for aqueous ZIBs. Ultrafine 4-6 nm MnO_2 nanocrystals were successfully wrapped in the organic PDAAQ matrix forming a mosaic structure. Surprisingly, an impressive high capacity of 414 mAh g^{-1} has been achieved in this novel MnO_2/PDAAQ composite, superior to most of conventional cathode materials. We revealed the storage mechanism of our MnO_2/PDAAQ cathode combines two main categories including Zn^{2+}/H^+ co-insertion in MnO_2, and dissolution/deposition mechanism of Mn^{4+}/Mn^{2+} redox reaction, thus resulting in much improved battery performances. As a proof-of-concept, when assembled in a full-cell with Zn anode, our MnO_2/PDAAQ cathode exhibits a superior energy density of 537.9 Wh kg^{-1} with long-term cycling life exceeds 2000 cycles with coulombic efficiency of 97%.

2. Results and discussion

Fig. 1a schematically illustrates our interfacial polymerization strategy for the synthesis of MnO_2@PDAAQ composites. In this

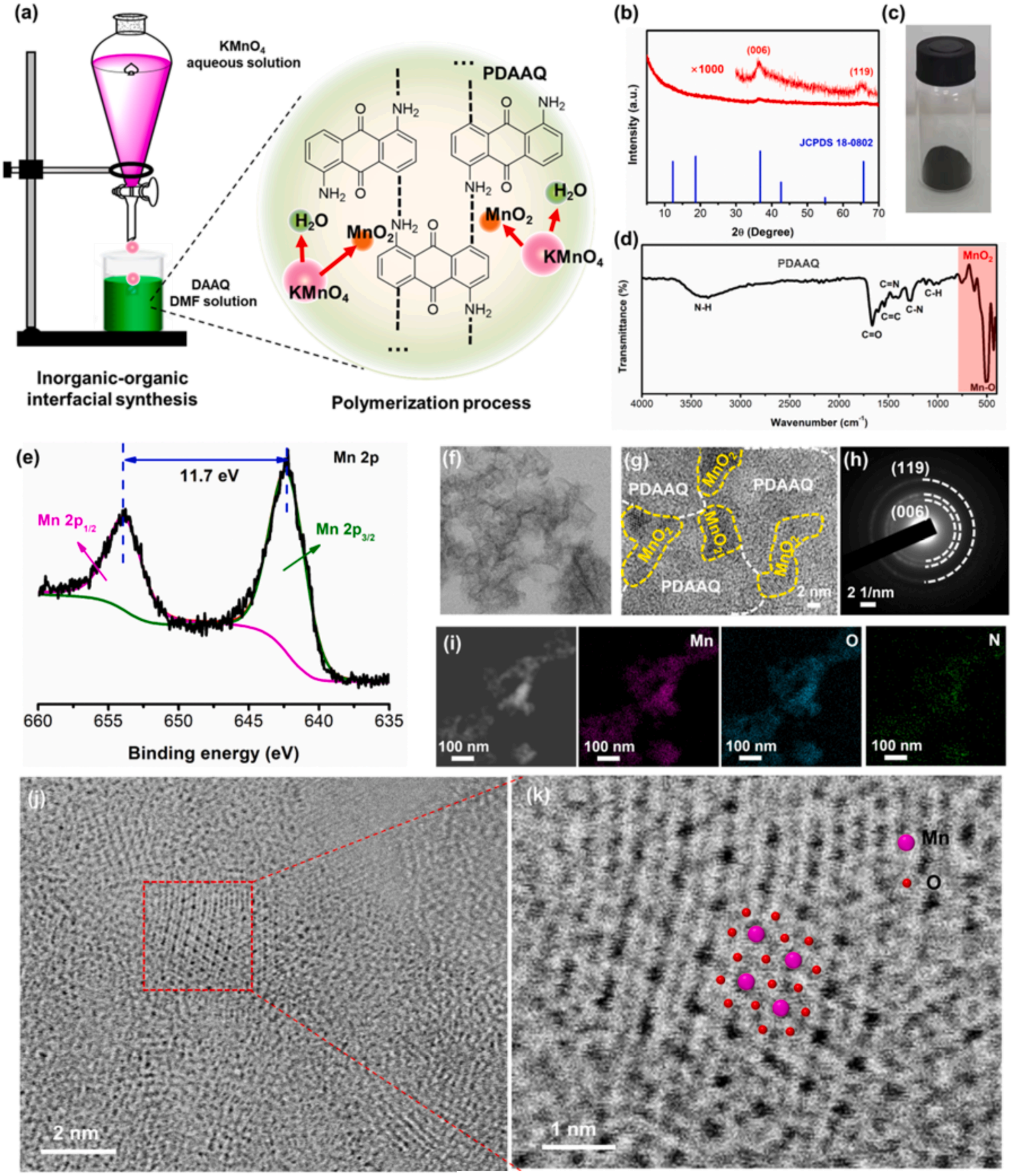

Fig. 1. (a) Schematic illustration of the preparation process. (b) Powder XRD pattern and (c) its optical photograph. (d) FTIR spectra. (e) High-resolution Mn 2p XPS spectra. (f, g) HRTEM images and (h) the corresponding SAED image. (i) Elemental mapping of Mn, N and O. (j, k) BF-STEM images.

synthesis, oxidizing agent (aqueous 3 g μL^{-1} $KMnO_4$ solution) was slowly dropped into the organic phase (DMF-containing diaminoanthraquinone monomer). Subsequently, PDAAQ was synthesized by the chemical oxidation polymerization and $KMnO_4$ was reduced to MnO_2 simultaneously. Powder X-Ray diffraction (XRD) pattern and Fourier transform infrared (FT-IR) spectra (Fig. 1b and d) confirm the successful formation of MnO_2@PDAAQ composites with black powder sample (Fig. 1c). Although XRD pattern exhibits rather broad peaks with poor crystallinity, the enlarged one from 30° to 70° clearly shows two diffraction peaks at 36.5 and 65.8^o, which well matches the (006) and (119) planes of layered birnessite phase (JCPDS:18-0802), respectively. FT-IR spectra in Fig. 1d depicts clear fingerprint peaks of PDAAQ in the composite [26–28]. Furthermore, the characteristic peak around 510 cm^{-1} can be ascribed to the Mn-O vibrations of [MnO_6] octahedra [15]. Similar results are also observed in the Raman spectrum (Fig. S1). The symmetric stretching vibration (Mn-O) of MnO_6 groups and the (Mn-O) stretching vibration in the basal plane of [MnO_6] sheet can be respectively detected at 640 and 570 cm^{-1} [29]. We further identify the PDAAQ content of approximately 23 wt % by thermogravimetric analysis (TGA) measurement (Fig. S2). Additionally, X-ray photoelectron spectra (XPS) further confirms the valence state of Mn in the composite. As depicted in Fig. 1e, the characteristic peak located at 642.3 and 654.0 eV are attributed to Mn $2p_{3/2}$ and Mn $2p_{1/2}$, respectively. The spin–orbit splitting of 11.7 eV matches well with the typical MnO_2 spectra in the previous work [30]. Furthermore, the average oxidation state of MnO_2 is calculated to be +4 through the relationship between the valence state

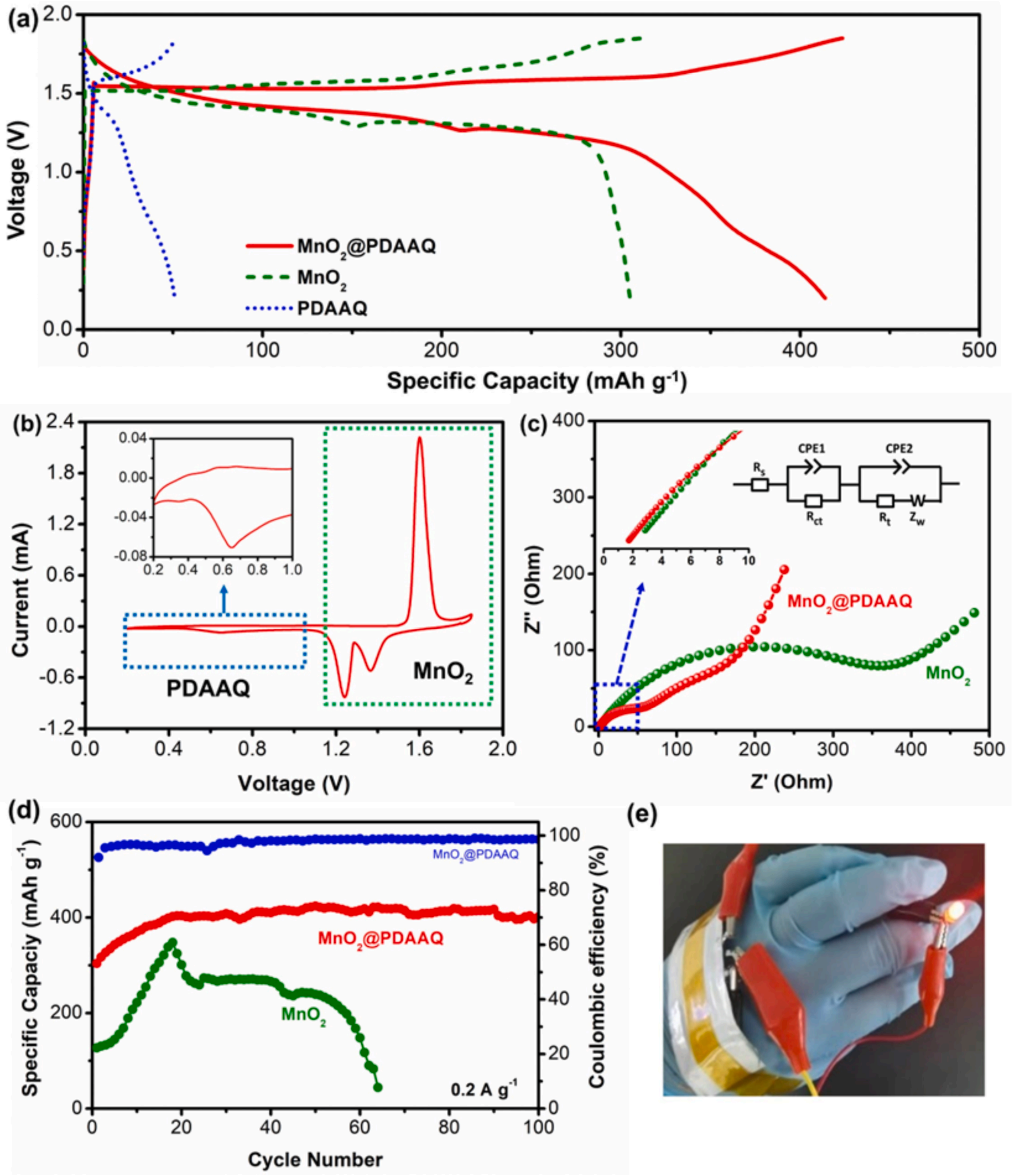

Fig. 2. (a) GCD profile of MnO_2@PDAAQ, MnO_2 and PDAAQ cathodes in 2 M $ZnSO_4$ /0.2 M $MnSO_4$ electrolyte at 0.2 A g^{-1} after activation process. (b) CV curve at 0.2 mV s^{-1}. (c) Nyquist plots at 1.5 V (inset illustrates equivalent circuit served for fitting EIS spectra). (d) Cycle performance in 2 M $ZnSO_4$/0.2 M $MnSO_4$ at 0.2 A g^{-1}. (e) A fully-charged pouch cell of two batteries in series can easily light up the red LED.

and the Mn 3s peak splitting energy as reported previously (Fig. S3) [31].

Scanning electron microscopy (SEM) observation of our MnO_2@PDAAQ composite shows a loose, spongiform morphology by the aggregation of numerous tiny nanoparticles (Fig. S4). Such a loose morphology gives rise to rather porous structure with a very high specific surface area of 234.9 $m^2\ g^{-1}$ (pore volume: 0.933 $cm^3\ g^{-1}$) evident by N_2 absorption-desorption isotherm (Fig. S5). Note the surface area of MnO_2@PDAAQ composite is remarkably higher than that of pristine MnO_2 nanoparticles (13.5 $m^2\ g^{-1}$) with drastic agglomeration [32], which generally facilitates the electron transfer at the electrode/electrolyte interface to promote electrochemical kinetics for battery applications. High-resolution transmission electron microscopy (HRTEM) observation further indicates continuous network structure constructed by the cross-linked polymer chains (Fig. 1f). Especially, ultrafine 4-6 nm MnO_2 nanocrystals can be easily distinguish in the high-resolution TEM image (Fig. 1g). It seems that the organic PDAAQ matrix is inlaid with the ultrafine MnO_2 nanocrystals forming a mosaic structure, which should be ascribed to the spacing confinement effect of PDAAQ macromolecules during the polymerization process. As a comparison, the morphology of pure MnO_2 prepared via a similar method without shows large-sized particles caused by the severe aggregation (> 1 μm, Fig. S6). The corresponding selected-area electron diffraction (SAED) pattern (Fig. 1h) exhibits a set of well-resolved birnessite diffraction rings, suggesting the polycrystalline nature of MnO_2 sub-phase in the composites. Elemental mapping images (Fig. 1i) illustrated a homogeneous distribution of Mn, N and O elements. We further carried out bright-field scanning transmission electron microscope (BF-STEM) characterization to identify the crystallographic information of these ultrafine MnO_2 nanocrystals. As shown in Fig. 1j, k, the atomic arrays marked by rectangle clearly indicate $[MnO_6]$ octahedron in which Mn atoms are coordinated by six adjacent lattice oxygen atoms, confirming layered birnessite structure of manganese oxide in the composite. This result is well consistent with the XRD characterization as shown in Fig. 1b. Furthermore, the PDAAQ matrix with amorphous structure can be clearly observed around MnO_2 nanocrystals in the BF-STEM images [33].

Having successfully prepared the highly uniform MnO_2@PDAAQ composite, it was paired against zinc foil using 2 M $ZnSO_4$/0.2 M $MnSO_4$ aqueous electrolyte to evaluate electrochemical properties. Fig. 2a compares the galvanostatic charge/discharge (GCD) profiles of the MnO_2@PDAAQ composite, MnO_2 and PDAAQ cathode after the activation process (discussed below). Intriguingly, we observed an apparent enhancement on capacity of our MnO_2@PDAAQ compared with the pristine MnO_2 (305 $mAh\cdot g^{-1}$) and PDAAQ cathode (51 $mAh\cdot g^{-1}$). CV curve in Fig. 2b indicates the onset of electrochemical activity starts just below 1.6 V, and there are two capacity regions that should be respectively assigned to MnO_2 (1.6−0.8 V) and PDAAQ (0.8−0.2 V) contribution, which is well consistent with the charge and discharge plateaus observed in the GCD profile of MnO_2@PDAAQ cathode. The electrochemical impedance spectroscopy (EIS) measurements in Fig. 2c delivers much smaller contact resistance as well as charge-transfer resistance of MnO_2@PDAAQ cathode than those of pristine MnO_2 (see Table S1), indicating the faster electrochemical reaction kinetics of the MnO_2@PDAAQ composite. As shown in Fig. 2d, MnO_2@PDAAQ cathode delivered better cycling stability than that of pure MnO_2 cathode in 2 M $ZnSO_4$/0.2 M $MnSO_4$ hybrid electrolyte. The initial capacity of MnO_2@PDAAQ sample is 303 $mAh\cdot g^{-1}$, and a gradual capacity rise in the first 20 cycles was observed, which should be ascribed to the mass increase of active MnO_2 originating from the deposition of Mn^{2+} in $MnSO_4$ during this activation process (Fig. S7) [34,35]. MnO_2@PDAAQ cathode delivers a high specific capacity of 414 mAh g^{-1} based on the mass of MnO_2@PDAAQ after activation (Figs. S8 and S9), and it maintained with a high capacity-retention of about 96% in the subsequent 100 cycles. Note that such a capacity of 414 mAh g^{-1} is much higher than most of the as-reported zinc-ion battery cathode materials up to date [7,9,15,17–20,36–53]. Long-term cycling lifespan of our MnO_2@PDAAQ sample is further confirmed at a high current density of 3.0 A g^{-1} with a stable capacity of ~100 mAh g^{-1} and coulombic efficiency of 97% after 2200 cycles (Fig. S10). Fig. S11 depicts its rate-capability at various current densities from 0.2 to 3.0 A g^{-1}. The reversible capacity is 372.9, 342.6, 306.2, 200.4 and 110.4 mAh g^{-1} at a current density of 0.2, 0.5, 1, 2 and 3 A g^{-1}, respectively. While the current density was set back to 0.2 A g^{-1}, the capacity delivers satisfactory reversibility and quickly raised to the capacity of 404.1 mAh g^{-1}. This excellent performance inspires us to further assemble a soft package of two batteries in series to verify its practical application in flexible and wearable device. As shown in Fig. 2e, the as-constructed pouch cell can be wound around the hand and light up a red LED indicator easily.

Fig. 3a depicts the comparison of specific capacity vs. average discharge voltage. Clearly, the overall performance on capacity and working voltage of our MnO_2@PDAAQ cathode exceeds most of conventional cathode materials including Mn-based compounds, V-based compounds, phosphates, sulfides, organics and Prussian blue analogues [7,9,15,17–20,36–53]. Benefited from this ultrahigh specific capacity, a prominent energy density of 537.9 Wh kg^{-1} (calculated based on the mass of MnO_2@PDAAQ) at a power density of 272.8 W kg^{-1} has been achieved, which is also much superior to conventional AZIBs cathodes including $VOPO_4$ [46], $V_3O_7\cdot nH_2O$ [47], α-MnO_2 [48], δ-MnO_2 [49], $ZnMn_{1.86}O_4$ [50], ZnHCF [51] and CuHCF [52] (Fig. 3b).

We have achieved satisfactory specific capacity and energy density in our MnO_2@PDAAQ composite. To gain the deep insights on the energy storage mechanism, *ex-situ* XRD was employed to investigate the composition change of MnO_2@PDAAQ composite cathode during the charge and discharge processes, which were carefully rinsed with deionized water to remove the electrolyte. Fig. 4a exhibits the XRD pattern of selected points in the GCD curve for *ex situ* analysis in the 10th cycle. The typical diffraction peaks assigned to $Zn_4SO_4(OH)_6\cdot nH_2O$ (ZHS, JCPDS: 44-0673 and 39-0689) could be observed from C to E point during the discharging process. In addition, the XRD diffraction peaks assigned to the MnOOH phase could also be found in the fully discharged cathode (E point) as shown in Fig. 4b. According to the previous reports, the insertion mechanism of H^+ are usually accompanied by the formation of ZHS and MnOOH [54]. Furthermore, the insertion mechanism of Zn^{2+} is confirmed by the appearance of the $ZnMn_2O_4$ phase at E point and the element mapping result (Fig. S12).

However, the theoretical capacity of MnO_2 based on the insertion mechanism is just 308 mAh g^{-1}, which is much lower than the capacity of our MnO_2@PDAAQ. The reason was further investigated by the *ex-situ* XPS and X-ray absorption near edge structure (XANES) characterizations, which confirmed a typical Mn^{4+}/Mn^{2+} dissolution/deposition mechanism during the charge-discharge process. Fig. 4c shows the normalized Mn K-edge XANES spectra of MnO_2@PDAAQ sample at various discharge/charge states (20th cycle) as marked in Fig. 4d. Commercial MnO_2 and Mn_2O_3 are used as reference samples. The edge gradually shifts toward higher energy during the discharging process (from A' to C' point), indicating a slight increase of the average Mn oxidation state in the cathode. Such an illogical variation trend of Mn valence has also been reported in previous work on MnO_2@V_2CT_X and MnO_x@N-C cathodes for AZIBs [34,55]. The reasonable explanation for this phenomenon could be the Mn^{3+} (MnOOH) disproportionate transformation into Mn^{4+} (Zn_2MnO_4, Fig. 4b), leaving Mn^{2+} dissolved into the electrolyte (e.g. $Mn^{3+}\rightarrow Mn^{4+} +$ *dissolved* Mn^{2+}). Moreover, the signal intensity of Mn K-edge at E' point is extremely weak below the detection limit (Fig. S13), suggesting the dissolution of most Mn component in the cathode after full discharging. The occurrence of Mn^{2+} dissolution during the discharging process is also confirmed by Fourier transformed Mn K-edge extended X-ray absorption fine structure (EXAFS) data. One can see the intensity of Mn-Mn_{edge} Fourier transforms peak (~1.8 Å) of C' point is much lower than that of B' point (~2.5 Å, Fig. S14) [56]. At full charged H' point, the K edge position almost returns to the initial A' point. Furthermore, the interatomic distance of

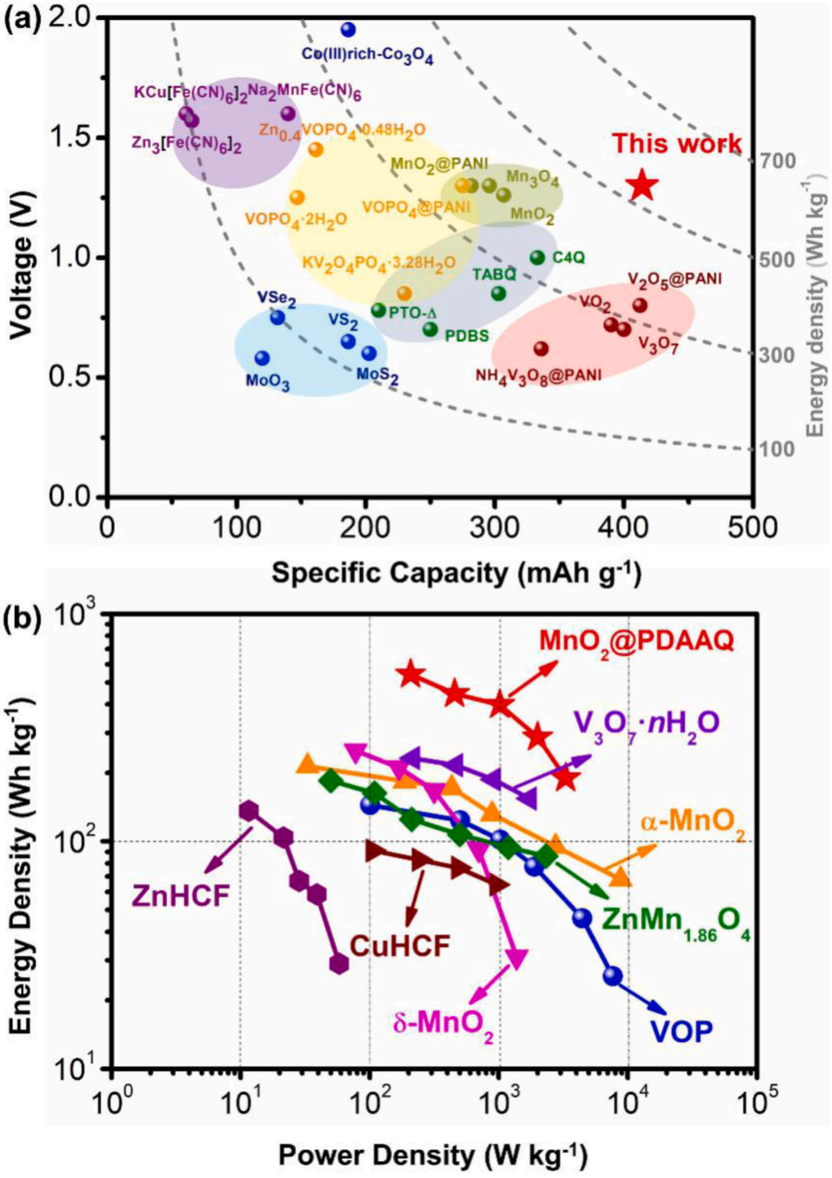

Fig. 3. (a) Performance comparison on specific capacities and average discharge voltage between our work and previously reported cathodes for ZIBs [7,9,15,17–20,36–53]. (b) Ragone plots compared to other cathodes of ZIBs [46–52].

Mn–O bond after this discharge/charge cycle shows negligible change in the EXAFS spectroscopy (Fig. S14), demonstrating excellent structural reversibility without remarkable changes on coordination geometry of our MnO_2@PDAAQ. *Ex-situ* XPS spectra in Fig. 4d also elucidates the Mn oxidation state evolution during this electrochemical process. The intensity of Mn 2p characteristic peaks gradually decreased from A' to E' point during the discharge process, and it was hardly distinguished at fully discharged E' point. Such a result also provides evidence of Mn dissolution from the MnO_2@PDAAQ cathode into liquid electrolyte. The high-resolution Mn 2p XPS spectra in Fig. 4e, f provide more detailed information. At the first discharge platform (A' to B') in the GCD profile, partial Mn^{4+} was converted to Mn^{3+} intermediate via the H^+ redox reaction. After this, the characteristic peaks at 641.2 and 653.3 eV assigned to Mn^{2+} replace those of Mn^{3+} (643.3 and 654.9 eV) and Mn^{4+} (642.3 and 654.0 eV) from C' to F' point. The emergence of Mn^{2+} is also proved by Mn 3s XPS spectra (Fig. S15), in which the energy separation of the characteristic peak is ~5.9 eV, corresponding a charge state of Mn^{2+} in these stages [32,57]. In contrast, the valence state of Mn in the pure MnO_2 cathode was confirmed to be between +3 and +4 at C point by the high-resolution XPS spectra (Fig. S16). During the subsequence charge process, the chemical valence of Mn changes back from +2 to +4 (Fig. 4f), which is in agreement with the above-mentioned XANES results.

Although pure PDAAQ also hold Zn^{2+} storage ability through a Zn^{2+}-coordination mechanism reported in previous reports on quinone compounds [17–20,58], the capacity comparison in Fig. 2a identifies that the capacity of our MnO_2@PDAAQ composite is dominated by the contribution of Mn species rather than PDAAQ. According to the abovementioned *ex situ* analyses, it rational that its high capacity should be attributed to the hybrid mechanisms including Zn^{2+}/H^+ co-insertion and dissolution/deposition of Mn^{4+}/Mn^{2+} redox reaction, which is schematically illustrated in Fig. 5 and summarized as following equations:

Cathode side:

(i) Zn^{2+}/H^+ co-insertion mechanism:

$$MnO_2 + H^+ + e^- \leftrightarrow MnOOH$$

$$2MnO_2 + Zn^{2+} + 2e^- \leftrightarrow ZnMn_2O_4$$

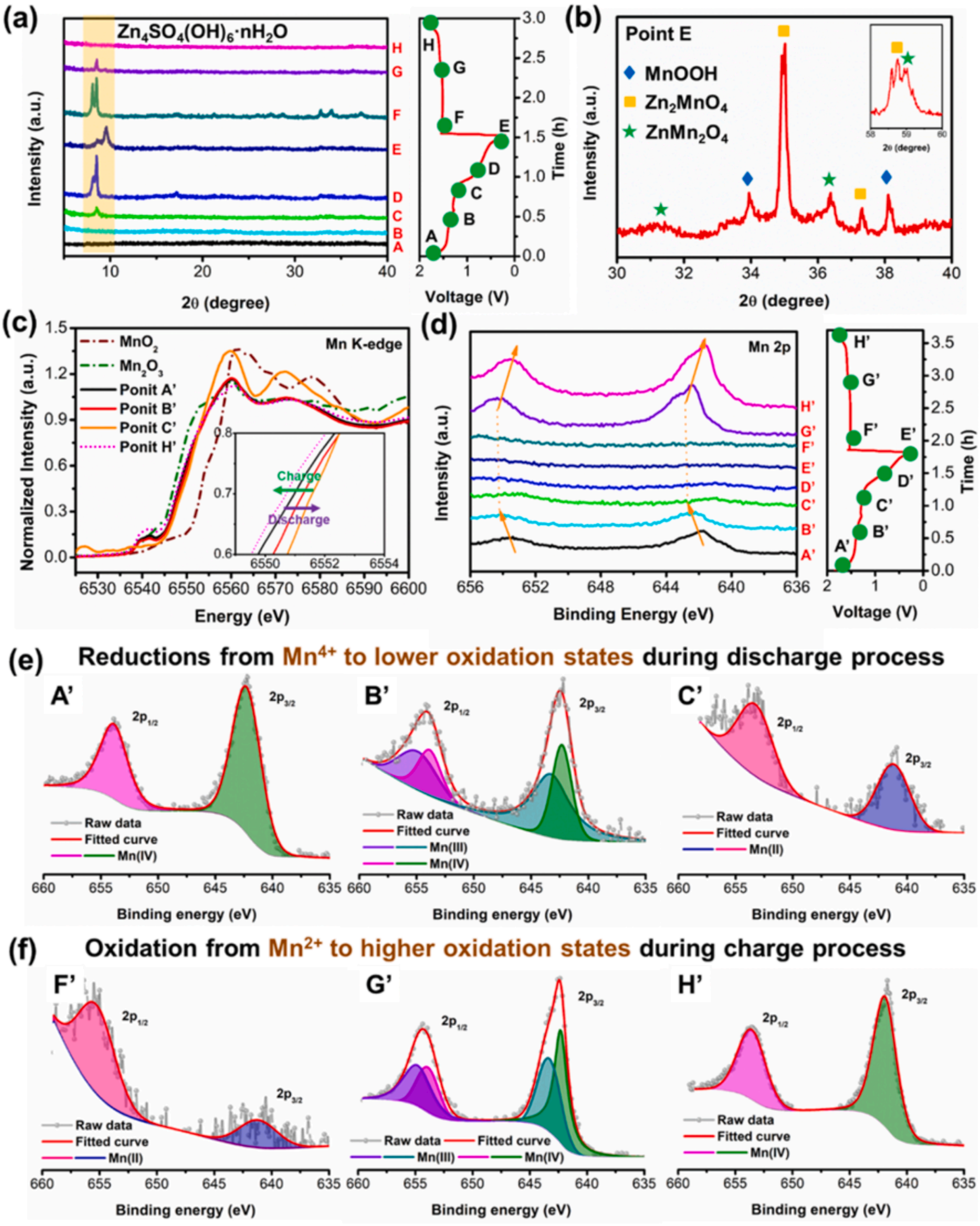

Fig. 4. XRD patterns at (a) various discharging/charging states and (b) E point in the 10th cycle of the MnO_2@PDAAQ cathode followed by a washing process of acetate buffer solution to completely remove ZHS byproduct. (c) Mn K-edge XANES and (d) Mn 2p XPS spectra of selected stages in the 20th cycle. High-resolution Mn 2p XPS spectra during (d) discharge process (A' to C') and charge process (F' to H').

$$4Zn^{2+} + 6OH^- + SO_4^{2-} + nH_2O \leftrightarrow Zn_4SO_4(OH)_6 \cdot nH_2O$$

(ii) Mn dissolution/deposition mechanism:

$$MnO_2 + H^+ + e^- \leftrightarrow MnOOH$$

$$2MnOOH + 2Zn^{z2+} \leftrightarrow Zn_2MnO_4 + Mn^{2+} + 2H^+$$

Anode side:

$$Zn \leftrightarrow Zn^{2+} + 2e^-$$

Note that Mn ion dissolution-deposition process corresponds to a two-electron dissolution/deposition mechanism with a very high theoretical capacity of 616 mAh g^{-1}, and it generally occurs reversibly in a strong acidic electrolyte condition, which would result in severe corrosion of Zn foil and structural collapse of the battery system [59,60]. Interestingly, our study demonstrates the observation in a mild

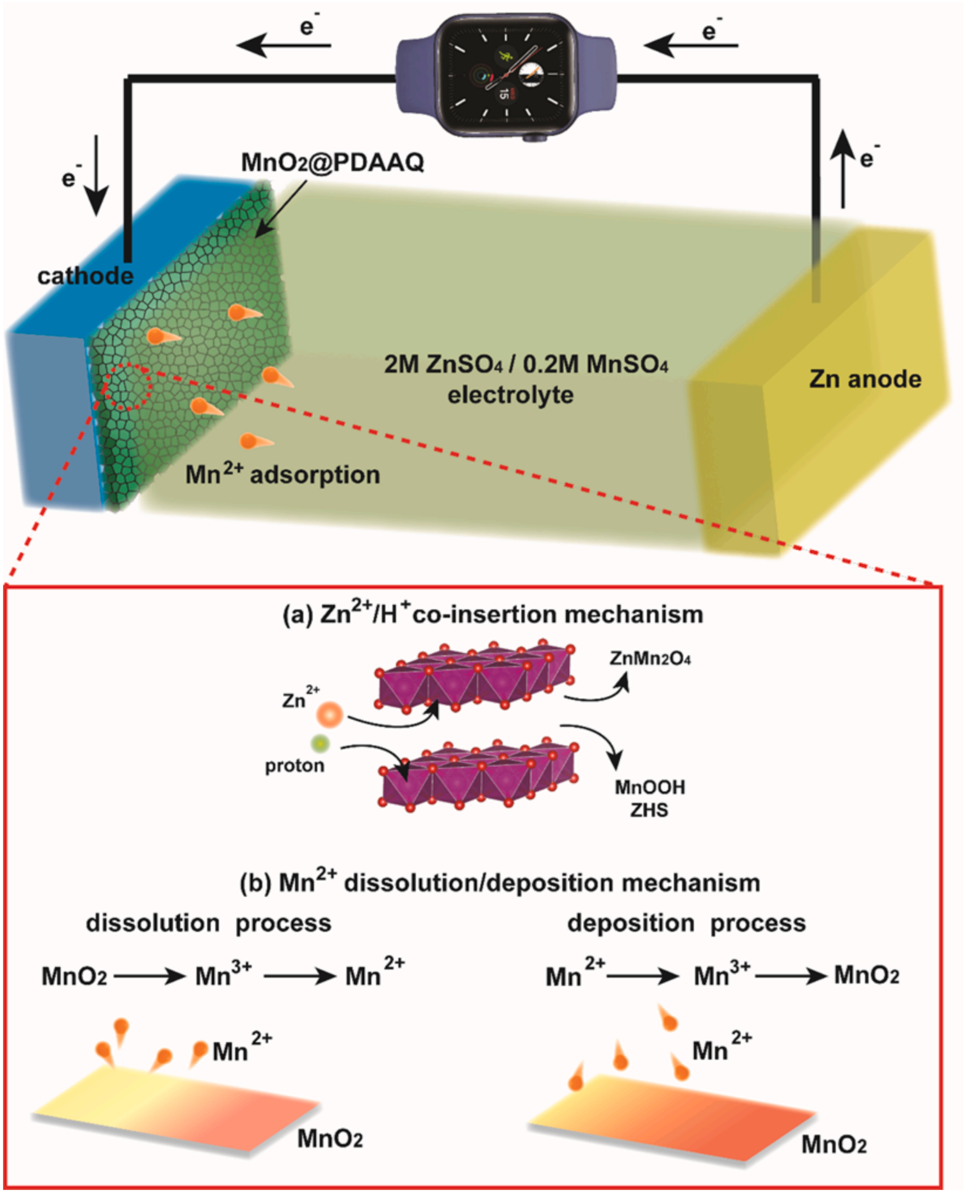

Fig. 5. Schematic diagram of the energy storage mechanism of MnO_2@PDAAQ composite in 2.0 M $ZnSO_4$/ 0.2 M $MnSO_4$ aqueous electrolyte.

electrolyte environment (2 M $ZnSO_4$/0.2 M $MnSO_4$, pH ≈ 4.6). Although the real reason is still not clear yet, we speculate that the strong absorption of Mn^{2+} on PDAAQ should drastically facilitate this high-capacity mechanism. To verify this hypothesis, the cyclic voltammetry was firstly employed. Unexpectedly, the CV curve of pure PDAAQ cathode in $ZnSO_4$/$MnSO_4$ hybrid aqueous electrolyte is quite different from that in $ZnSO_4$ electrolyte (Fig. S17). After several cycles, an anodic peak at 1.6 V and cathodic peaks at 1.36 and 1.2 V respectively emerges in the CV curves while pure PDAAQ cathode cycled in the $ZnSO_4$/$MnSO_4$ aqueous electrolyte, which corresponds to the redox characteristic peaks of MnO_2. This result indicates that the Mn^{2+} additive in the electrolyte could be deposited on the PDDAQ matrix, which is originated from the effective Mn^{2+} adsorption of the PDAAQ molecules. Typical high-resolution XPS spectrum of Mn 2p belong to MnO_2 phase could be found in the pure PDDAQ cathode after 100 cycles (Fig. S18), further providing evidence to support this inference. Density functional theory (DFT) simulation further provides evidence on the Mn^{2+} absorption effect with the presence of PDAAQ matrix. Firstly, the electrostatic potential surface of PDAAQ was simulated to expose the electrochemical active sites for cation chelation. Calculation results clarify the area around the carbonyl (C=O) and imino (-NH-) groups are electronegativity as favorable active sites capable of enhancing cation uptake (Fig. S19). Subsequently, after geometric optimization for structure of PDAAQ organic molecules (Fig. S20), the surface adsorption of Mn^{2+} by carbonyl and amino groups in PDAAQ is thermodynamically feasible with a negative binding energy (E_b) of -2.33 eV. Such a result also confirms the strong Mn^{2+} adsorption on PDAAQ surface.

Additionally, we observed that the pure MnO_2 cathode shows a capacity fading due to the irreversible dissolution of Mn^{2+} in 2 M $ZnSO_4$ aqueous electrolyte without $MnSO_4$ additive as shown in Fig. S21 [34, 52]. In contrast, MnO_2@PDAAQ cathode delivered the relieving of capacity deterioration in the same condition, which provides another evidence for such an enhanced reversibility of Mn^{2+} dissolution-deposition process originated from PDAAQ. Generally, on the basis of the Nernst equation as follows: [60]

$$E = E^{0'} - \frac{RT}{zF} ln \frac{C_{Mn^{2+}}}{C_{MnO_2}} = E^{0'} - \frac{RT}{zF} lnC_{Mn^{2+}}$$

The equilibrium deposition potential depends on the concentration of Mn^{2+} in the electrolyte. During the discharging process, the electronegative PDAAQ molecules adsorb Mn^{2+} from the electrolyte and reduce the Mn^{2+} concentration in the cathode/electrolyte interface, which promotes the MnO_2 dissolution process to balance the net negative charge due to the Zn^{2+} insertion into MnO_2. Reversely, the as-adsorbed Mn^{2+} will be released from PDAAQ matrix with the Zn^{2+} extraction in the charging process as supported by the enhanced Mn-O characteristic peak in the FTIR spectra upon charging to 1.85 V compared to the discharging state (Fig. S22), thus enhancing the reversibility of Mn dissolution-deposition and leading to a highly stable capacity during the long-term cycling [61].

3. Conclusion

We demonstrated manganese oxide/quinone (MnO_2@PDAAQ) composite is a very appealing cathode candidate for aqueous zinc-ion battery with a high specific capacity of 414 mAh g^{-1}. Systematic study by *ex-situ* XRD, XPS, XANES and reveals hybrid energy storage mechanisms including Zn^{2+}/H^+ co-insertion in MnO_2, and two-electron dissolution/deposition mechanism of Mn^{4+}/Mn^{2+} redox reaction in this composite. Theoretical simulation suggests PDAAQ matrix plays a key role on the regulation of Mn-ion concentration, which is favorable for improving the reversibility of dissolution/deposition mechanism to realize a superior the specific capacity. Our inorganic oxide/organic quinone coupling strategy opens up a new route to break through the aqueous ZIBs performance limit on capacity and energy density, and it could also be extended to other quinone molecules. In the next work, we will continue to optimize the battery performance by regulation of the composition and structure of quinone compounds in this composited electrode.

4. Experimental section

4.1. Synthesis of MnO_2@PDAAQ sample

The MnO_2@PDAAQ sample is synthesized by an interfacial oxidative polymerization. Typically, 2 g 1,5-DAAQ monomer was dissolved in 100 mL dimethyl formamide (DMF), and 0.3 g $KMnO_4$ was dissolved in 100 mL deionized water, simultaneously. $KMnO_4$ aqueous solution was slowly dripped into the stirred organic solution in 6 h and followed by stirring for 24 h. Whereafter, the precipitate was collected by vacuum filtration followed by washing with 1-methyl-2-pyrrolidinone (NMP) and deionized water to remove the oligomers, monomer, and oxidant. Finally, the as-prepared MnO_2@PDAAQ was dried in an oven at 80 °C overnight. As comparison, pristine MnO_2 counterpart was prepared by a classical redox reaction between $MnSO_4$ and $KMnO_4$ in the similar route (detailed characterizations are shown in Fig. S23), and the pure PDAAQ was polymerization via 1,5-DAAQ monomer and $KMnO_4$ oxidant in acid environment.

4.2. Materials characterization

X-ray diffraction (Shimadzu XRD-6100) was performed to investigate the phase structure of the samples. X-ray photoelectron spectroscopy (XPS, Thermo 250 xi) was used to characterize the chemical compositions and element valence of the samples. The morphology and energy dispersive X-ray spectroscopy (EDX elemental analysis) of the samples were studied by field-emission scanning electron microscopy (FE-SEM, ZEISS SIGMA HD) and transmission electron microscopy JEM ARM200F (JEOL, Tokyo, Japan). Fourier transform infrared (FT-IR) spectra using KBr pellets (BRUKER, TENSOR II) and Raman spectroscopy (Renishaw Invia) were used to identify the structural variations in the samples. The nitrogen adsorption-desorption isotherm was studied by an Autosorb iQ instrument at 77 K. Thermogravimetric analysis (TGA) combined with differential thermal gravity (METTLER TGA2) was used to study the mass ratios of components. A four-probe resistivity tester (ST2722) were used to measure the electronic conductance of samples. The Mn K-edge XANES spectra were studied at Shanghai Synchrotron Radiation Facility. The samples were wrapped in clear polyimide tape and the data are normalized by *Athena*.

4.3. Electrochemical measurement

Working electrodes are prepared by mixing as-prepared samples, Ketjen black and PVDF with weight ratio of 7:2:1 in NMP to form homogeneous slurry, followed by coating onto a stainless-steel foil and drying at 60 °C for 12 h in a vacuum oven. The cut foil was served as the cathode (mass loading ~1.5 mg cm^{-2}), while the zinc foil and glass fiber membrane were used as the anode and separator, respectively, and 50 μL 2 M $ZnSO_4$/0.2 M $MnSO_4$ was employed as the electrolyte. The whole battery was assembled in a CR2032-type coin cell with the beforehand electrodes and other relevant components. Computer-controlled LAND battery test system (CT2001A) was used to evaluate the cell performances at room temperature. Cyclic Voltammetry test was performed at different sweep rate and electrochemical impedance spectroscopy (EIS) from 100 kHz to 100 mHz on an electrochemical workstation (CHI660E), respectively.

Supporting information

Supporting Information is available from the Elsevier Online Library or from the author.

CRediT authorship contribution statement

Fei Ye: Investigation, Data curation, Writing – original draft. **Qiang Liu:** Investigation, Validation, Writing – original draft. **Chengjie Lu:** Conceptualization, Software. **Fanqi Meng:** Investigation, Data curation. **Ting Lin:** Investigation, Data curation. **Hongliang Dong:** Investigation, Data curation. **Lin Gu:** Project administration, Writing – review & editing. **Yuping Wu:** Investigation, Project administration. **Zilong Tang:** Investigation, Project administration. **Linfeng Hu:** Supervision, Project administration, Methodology, Conceptualization, Writing – review & editing.

Declaration of Competing Interest

The authors declare that they have no known competing financial interests or personal relationships that could have appeared to influence the work reported in this paper.

Data availability

Data will be made available on request.

Acknowledgement

This work was financially supported by the National Key Research and Development Program of China (Grant No. 2021YFB2400400), the National Natural Science Foundation of China (51872051, 52171203), the Natural Science Foundation of Jiangsu Province (Grants No. BK20211516), the State Key Laboratory of New Ceramic and Fine Processing of Tsinghua University (No. KF202102), and the Fundamental Research Funds for the Central Universities (2242021R10119).

Supplementary materials

Supplementary material associated with this article can be found, in the online version, at doi:10.1016/j.ensm.2022.08.040.

References

[1] L.E. Blanc, D.L. Kundu, F. Nazar, Scientific challenges for the implementation of Zn-ion batteries, Joule 4 (2020) 771.

[2] Y.L. Liang, H. Dong, D. Aurbach, Y. Yao, Current status and future directions of multivalent metal-ion batteries, Nat. Energy 5 (2020) 646.

[3] N. Zhang, X.Y. Chen, M. Yu, Z.Q. Niu, F.Y. Cheng, J. Chen, Materials chemistry for rechargeable zinc-ion batteries, Chem. Soc. Rev. 49 (2020) 4203.

[4] X.X. Jia, C.F. Liu, Z.G. Neale, J.H. Yang, G.Z. Cao, Active materials for aqueous zinc ion batteries: synthesis, crystal structure, morphology, and electrochemistry, Chem. Rev. 120 (2020) 7795.

[5] Y.X. Zeng, X.F. Lu, S.L. Zhang, D.Y. Luan, S. Li, X.W. Lou, Construction of Co-Mn prussian blue analog hollow spheres for efficient aqueous Zn-ion batteries, Angew. Chem. Int. Ed. 60 (2021) 22189.

[6] W.J. Deng, Z.G. Li, Y.K. Ye, Z.Q. Zhou, Y.B. Li, M. Zhang, X.R. Yuan, J. Hu, W. G. Zhao, Z.Y. Huang, C. Li, H.B. Chen, J.X. Zheng, R. Li, Zn^{2+} induced phase transformation of $K_2MnFe(CN)_6$ boosts highly stable zinc-ion storage, Adv. Energy Mater. 11 (2021), 2003639.

[7] L.F. Hu, Z.Y. Wu, C.J. Lu, F. Ye, Q. Liu, Z.M. Sun, Principles of interlayer-spacing regulation of layered vanadium phosphates for superior zinc-ion batteries, Energy Environ. Sci. 14 (2021) 4095.

[8] W.J. Li, C. Han, Q.F. Gu, S.L. Chou, J.Z. Wang, H.K. Liu, S.X. Dou, Electron delocalization and dissolution-restraint in vanadium oxide superlattices to boost electrochemical performance of aqueous zinc-ion batteries, Adv. Energy Mater. (2020), 2001852.

[9] Z.Y. Wu, C.J. Lu, Y.N. Wang, L. Zhang, L. Jiang, W.C. Tian, C.L. Cai, Q.F. Gu, Z. M. Sun, L.F. Hu, Ultrathin VSe_2 nanosheets with fast ion diffusion and robust structural stability for rechargeable zinc-ion battery cathode, Small 16 (2020), 2000698.

[10] J.J. Wang, J.G. Wang, H.Y. Liu, Z.Y. You, Z. Li, F.Y. Kang, B.Q. Wei, A highly flexible and lightweight MnO_2/graphene membrane for superior zinc-ion batteries, Adv. Funct. Mater. 31 (2020), 2007397.

[11] Y. Zhang, S.J. Deng, Y.H. Li, B. Liu, G.X. Pan, Q. Liu, X.L. Wang, X.H. Xia, J.P. Tu, Anchoring MnO_2 on nitrogen-doped porous carbon nanosheets as flexible arrays cathodes for advanced rechargeable Zn-MnO_2 batteries, Energy Storage Mater. 29 (2020) 52.

[12] J.H. Song, K. Xu, N. Liu, D. Reed, X.L. Li, Crossroads in the renaissance of rechargeable aqueous zinc batteries, Mater. Today 45 (2021) 191.

[13] S.D. Liu, L. Kang, J.M. Kim, Y.T. Chun, J. Zhang, S.C. Jun, Recent advances in vanadium-based aqueous rechargeable zinc-ion batteries, Adv. Energy Mater. 10 (2020), 2000477.

[14] J.H. Huang, Z. Wang, M.Y. Hou, X.L. Dong, Y. Liu, Y.G. Wang, Y.Y. Xia, Polyaniline-intercalated manganese dioxide nanolayers as a high-performance cathode material for an aqueous zinc-ion battery, Nat. Commun. 9 (2018) 2906.

[15] Z.G. Yao, Q.P. Wu, K.Y. Chen, J.J. Liu, C.L. Li, Shallow-layer pillaring of a conductive polymer in monolithic grains to drive superior zinc storage via a cascading effect, Energy Environ. Sci. 13 (2020) 3149.

[16] X.M. Ma, X.X. Cao, M.L. Yao, L.T. Shan, X.D. Shi, G.Z. Fang, A.Q. Pan, B.A. Lu, J. Zhou, S.Q. Liang, Organic-inorganic hybrid cathode with dual energy storage mechanism for ultrahigh-rate and ultralong-life aqueous zinc-ion batteries, Adv. Mater. 34 (2022), 2105452.

[17] Q. Zhao, W.W. Huang, Z.Q. Luo, L.J. Liu, Y. Lu, Y.X. Li, L. Li, J.Y. Hu, H. Ma, J Chen, High-capacity aqueous zinc batteries using sustainable quinone electrodes, Sci. Adv 4 (2018) eaao1761.

[18] K.W. Nam, H. Kim, Y. Beldjoudi, T. Kwon, D.J. Kim, J.F. Stoddart, Redox-active phenanthrenequinone triangles in aqueous rechargeable zinc batteries, J. Am. Chem. Soc. 142 (2020) 2541.

[19] T. Sun, Z.J. Li, Y.F. Zhi, Y.J. Huang, H.J. Fan, Q.C. Zhang, Poly(2,5-Dihydroxy-1,4-Benzoquinonyl Sulfide) as an efficient cathode for high-performance aqueous zinc–organic batteries, Adv. Funct. Mater. 31 (2021), 2010049.

[20] Z.R. Lin, H.Y. Shi, L. Lin, X.P. Yang, W.L. Wu, X.Q. Sun, A high capacity small molecule quinone cathode for rechargeable aqueous zinc-organic batteries, Nat. Commun. 12 (2021) 4424.

[21] Z.W. Tie, Z.Q. Niu, Design strategies for high-performance aqueous Zn/organic batteries, Angew. Chem. Int. Ed. 59 (2020) 21293.

[22] Y.J. Gao, G.F. Li, F. Wang, J. Chu, P. Yu, B.S. Wang, H. Zhan, Z.P. Song, A high-performance aqueous rechargeable zinc battery based on organic cathode integrating quinone and pyrazine, Energy Storage Mater. 40 (2021) 31.

[23] Y.R. Wang, C.X. Wang, Z.G. Ni, Y.M. Gu, B.L. Wang, Z.W. Guo, Z. Wang, D. Bin, J. Ma, Y.G. Wang, Binding zinc ions by carboxyl groups from adjacent molecules toward long-life aqueous zinc-organic batteries, Adv. Mater. 32 (2020), 2000338.

[24] X.Y. Wu, J.J. Hong, W. Shin, L. Ma, T.C. Liu, X.X. Bi, Y.F. Yuan, Y.T. Qi, T.W. Surta, W.X. Huang, J. Neuefeind, T.P. Wu, P.A. Greaney, J. Lu, X.L. Ji, Diffusion-free grotthuss topochemistry for high-rate and long-life proton batteries, Nat. Energy 4 (2019) 123.

[25] L. Jiang, Z.Y. Wu, Y.N. Wang, W.C. Tian, Z.Y. Yi, C.L. Cai, Y.C. Jiang, L.F. Hu, Ultrafast zinc-ion diffusion ability observed in 6.0-nanometer spinel nanodots, ACS Nano 13 (9) (2019) 10376.

[26] H.Y. Liu, G.Q. Zhang, C.Q. Zhao, J.D. Liu, F.L Yang, Hydraulic power and electric field combined antifouling effect of a novel conductive poly (aminoanthraquinone)/reduced graphene oxide nanohybrid blended PVDF ultrafiltration membrane, J. Mater. Chem. A 3 (2015) 20277.

[27] N. An, Z.H. Shao, Z. Guo, J. Xin, Y.Y. He, L.W. Lv, K.F. Xie, X.Y. Dong, Y. Zhang, Z. G Hu, High energy-density supercapacitor based on a novel conjugated poly (1,5-diaminoanthraquinone)/intercalated graphene composite system, J. Power Sources 475 (2020), 228692.

[28] J Tian, X.J Zhou, Q.P. Wu, C.L. Li, Li-salt mediated Mg-rhodizonate batteries based on ultra-large cathode grains enabled by K-ion pillaring, Energy Storage Mater. 22 (2019) 218.

[29] S.B. Ma, Y.H. Lee, K.Y. Ahn, C.M. Kim, K.H. Oh, K.B Kim, Spontaneously deposited manganese oxide on acetylene black in an aqueous potassium permanganate Solution, J. Electrochem. Soc. 153 (2006) C27.

[30] B. He, Q.C. Zhang, L.H. Li, J. Sun, P. Man, Z.Y. Zhou, Q.L. Li, J.B. Guo, L.Y. Xie, C. W. Li, X.N. Wang, J.X. Zhao, T. Zhang, Y.G. Yao, High-performance flexible all-solid-state aqueous rechargeable Zn-MnO_2 microbatteries integrated with wearable pressure sensors, J. Mater. Chem. A 6 (2018) 14594.

[31] B.W. Lin, X.H. Zhu, L.Z. Fang, X.Y. Liu, S. Li, T. Zhai, L. Xue, Q.B. Guo, J. Xu, H Xia, Birnessite nanosheet arrays with high K content as a high-capacity and ultrastable cathode for K-ion batteries, Adv. Mater. 31 (2019), 1900060.

[32] X.Z. Zhai, J. Qu, S.M. Hao, Y.Q. Jing, W. Chang, J. Wang, W. Li, Y. Abdelkrim, H. F. Yuan, Z.Z. Yu, Layered birnessite cathode with a displacement/intercalation mechanism for high-performance aqueous zinc-ion batteries, Nano-Micro Lett. 12 (2020) 56.

[33] Y.Q. Meng, J.B. Fan, M.H. Wang, W.B. Gong, J.P. Zhang, J.P. Ma, H.Y. Mi, Y. Huang, S. Yang, R.S. Ruoff, J.X Geng, Encoding enantiomeric molecular chiralities on graphene basal planes, Angew. Chem. Int. Ed. 61 (2022), e202117815.

[34] X.D. Zhu, Z.Y. Cao, W.J. Wang, H.J. Li, J.C. Dong, S.P. Gao, D.X. Xu, L. Li, J. F. Shen, M.X. Ye, Superior-performance aqueous zinc-ion batteries based on the *in situ* growth of MnO_2 nanosheets on V_2CTX MXene, ACS Nano 15 (2021) 2971.

[35] H. Chen, C.L. Dai, F.Y. Xiao, Q.J. Yang, S.N. Cai, M.W. Xu, H.J. Fan, S.J. Bao, Reunderstanding the reaction mechanism of aqueous Zn–Mn batteries with sulfate electrolytes: role of the zinc sulfate hydroxide, Adv. Mater. 34 (2022), 2109092.

[36] Z.Y. Wu, Y.N. Wang, L. Zhang, L. Jiang, W.C. Tian, C.L. Cai, J. Price, Q.F. Gu, L. F. Hu, A layered $Zn_{0.4}VOPO_4{\cdot}0.8H_2O$ cathode for robust and stable Zn ion storage, ACS Appl. Energy Mater 3 (2020) 3919.

[37] S.C. Liu, H. Zhu, B.H. Zhang, G. Li, H.K. Zhu, Y. Ren, H.B. Geng, Y. Yang, Q. Liu, C. C. Li, Tuning the kinetics of zinc-ion insertion/extraction in V_2O_5 by *In situ* polyaniline intercalation enables improved aqueous zinc-ion storage performance, Adv. Mater. 32 (2020), 2001113.

[38] D. Bin, W.C. Huo, Y.B. Yuan, J.H. Huang, Y. Liu, Y.X. Zhang, F. Dong, Y.G. Wang, Y.Y Xia, Organic-inorganic-induced polymer intercalation into layered composites for aqueous zinc-ion battery, Chem 6 (2020) 968.

[39] Z.Y. Cao, L.P. Wang, H. Zhang, X. Zhang, J.W. Liao, J.C. Dong, J.Y. Shi, P. Y. Zhuang, Y.D. Cao, M.X. Ye, J.F. Shen, P.M. Ajayan, Localized ostwald ripening guided dissolution/regrowth to ancient chinese coin-shaped VO_2 nanoplates with enhanced mass transfer for zinc ion storage, Adv. Funct. Mater. 30 (2020), 2000472.

[40] Z.G. Hou, X.Q. Zhang, X.N. Li, Y.C. Zhu, J.W. Liang, Y.T Qian, Surfactant widens the electrochemical window of an aqueous electrolyte for better rechargeable aqueous sodium/zinc battery, J. Mater. Chem. A 5 (2017) 730.

[41] X. Yang, W.Z. Deng, M. Chen, Y.B. Wang, C.F. Sun, Mass-producible, quasi-zero-strain, lattice-water-rich inorganic open-frameworks for ultrafast-charging and long-cycling zinc-ion batteries, Adv. Mater. 32 (2020), 2003592.

[42] Y.Z. Lu, J. Wang, S.Q. Zeng, L.J. Zhou, W. Xu, D.Z. Zheng, J. Liu, Y.X. Zeng, X. H. Lu, An ultrathin defect-rich Co_3O_4 nanosheet cathode for high-energy and durable aqueous zinc ion batteries, J. Mater. Chem. A 7 (2019) 21678.

[43] T.P. Jiao, Q. Yang, S.L. Wu, Z.F. Wang, D. Chen, D. Shen, B. Liu, J.Y. Cheng, H.F. Li, L.T. Ma, C.Y. Zhi, W.J. Zhang, Binder-free hierarchical VS_2 electrodes for high-performance aqueous Zn ion batteries towards commercial level mass loading, J. Mater. Chem. A 7 (2019) 16330.

[44] T. Xiong, Y.X. Zhang, Y.M. Wang, W.S.V. Lee, J.M. Xue, Hexagonal MoO_3 as a zinc intercalation anode towards zinc metal-free zinc-ion batteries, J. Mater. Chem. A 8 (2020) 9006.

[45] W.W. Xu, C.L. Sun, K.N. Zhao, X. Cheng, S. Rawal, Y. Xu, Y. Wang, Defect engineering activating (boosting) zinc storage capacity of MoS_2, Energy Storage Mater. 16 (2019) 527.

[46] H.Y. Shi, Y. Song, Z.M. Qin, C.C. Li, D. Guo, X.X. Liu, X.Q. Sun, Inhibiting $VOPO_4{\cdot}xH_2O$ decomposition and dissolution in rechargeable aqueous zinc batteries to promote voltage and capacity stabilities, Angew. Chem. Int. Ed. 58 (2019) 16057.

[47] D.P. Kundu, S.H. Vajargah, L.W. Wan, B. Adams, D. Prendergast, L.F. Nazar, Aqueous vs. nonaqueous zn-ion batteries: consequences of the desolvation penalty at the interface, Energy Environ. Sci. 11 (2018) 881.

[48] C.J. Xu, B.H. Li, H.D. Du, F.Y. Kang, Energetic zinc ion chemistry: the rechargeable zinc ion battery, Angew. Chem. Int. Ed. 51 (2012) 933.

[49] M.H. Alfaruqi, J. Gim, S.J. Kim, J.J. Song, D.T. Pham, J. Jo, Z.L. Xiu, V. Mathew, J. Kim, A layered δ-MnO_2 nanoflake cathode with high zinc-storage capacities for eco-friendly battery applications, Electrochem. Commun. 60 (2015) 121.

[50] N. Zhang, F.Y. Cheng, Y.C. Liu, Q. Zhao, K.X. Lei, C.C. Chen, X.S. Liu, J. Chen, Cation-deficient spinel $ZnMn_2O_4$ cathode in $Zn(CF_3SO_3)_2$ electrolyte for rechargeable aqueous Zn-ion battery, J. Am. Chem. Soc. 138 (2016) 12894.

[51] L.Y. Zhang, L. Chen, X.F. Zhou, Z.P. Liu, Towards high-voltage aqueous metal-ion batteries beyond 1.5 V: the zinc/zinc hexacyanoferrate system, Adv. Energy Mater. 5 (2015), 1400930.

[52] R. Trocoli, F.L. Mantia, An aqueous zinc-ion battery based on copper hexacyanoferrate, ChemSusChem 8 (2015) 481.

[53] J.W. Hao, J. Mou, J.W. Zhang, L.B. Dong, W.B. Liu, C.J. Xu, F.Y. Kang, Electrochemically induced spinel-layered phase transition of Mn_3O_4 in high performance neutral aqueous rechargeable zinc battery, Electrochim. Acta 259 (2018) 170.

[54] W. Sun, F. Wang, S. Hou, C.Y. Yang, X.L. Fan, Z.H. Ma, T. Gao, F.D. Han, R.Z. Hu, M. Zhu, C.S. Wang, Zn/MnO$_2$ battery chemistry with H$^+$ and Zn^{2+} coinsertion, J. Am. Chem. Soc. 139 (2017) 9775.

[55] Y.Q. Fu, Q.L. Wei, G.X. Zhang, X.M. Wang, J.H. Zhang, Y.F. Hu, D.N. Wang, L. Zuin, T. Zhou, Y.C. Wu, S.H. Sun, High-performance reversible aqueous Zn-ion battery based on porous MnO$_x$ nanorods coated by MOF-derived N-doped carbon, Adv. Energy Mater. 8 (2018), 1801445.

[56] K.W. Nam, M.G. Kim, K.B Kim, *In Situ* Mn K-edge X-ray absorption spectroscopy studies of electrodeposited manganese oxide films for electrochemical capacitors, J. Phys. Chem. C 111 (2007) 749–758.

[57] W.G. Cui, X.Y. Zhuang, Y.T. Li, H.B. Zhang, J.J. Dai, L. Zhou, Z.P. Hu, T.L. Hu, Engineering Co/MnO heterointerface inside porous graphitic carbon for boosting the low-temperature CO$_2$ methanation, Appl. Catal. B Environ. 287 (2021), 119959.

[58] K.X. Huang, Z.G. Yao, K. Sun, K.Y. Chen, J.L. Hu, D.G. Yin, C.L. Li, Electrolyte formulation to enable ultra-stable aqueous Zn-organic batteries, J. Power Sources 482 (2021), 228904.

[59] D.L. Chao, W.H. Zhou, C. Ye, Q.H. Zhang, Y.G. Chen, L. Gu, K. Davey, S.Z. Qiao, An electrolytic Zn-MnO$_2$ battery for high-voltage and scalable energy storage, Angew. Chem. Int. Ed. 58 (2019) 7823.

[60] H. Moon, K.H. Ha, Y. Park, J. Lee, M.S. Kwon, J. Lim, M.H. Lee, D.H. Kim, J. H. Choi, J.H. Choi, K.T. Lee, Direct proof of the reversible dissolution/deposition of Mn^{2+}/Mn^{4+} for mild-acid Zn-MnO$_2$ batteries with porous carbon interlayers, Adv. Sci. 8 (2021), 2003714.

[61] X.S. Xie, H.W. Fu, Y. Fang, B.A. Lu, J. Zhou, S.Q. Liang, Manipulating ion concentration to boost two-electron Mn^{4+}/Mn^{2+} redox kinetics through a colloid electrolyte for high-capacity zinc batteries, Adv. Energy Mater. 12 (2022), 2102393.